Fast-slow dynamics in a memristive ion channel-based bionic circuit

Xincheng Ding[1] · Chengtao Feng[1] · Ning Wang[1] · Ao Liu[1] · Quan Xu[1]

Abstract

Electrophysiological properties of ion channels can influence the transport process of ions and the generation of firing patterns in an excitable biological neuron when applying an external stimulus and exceeding the excitable threshold. In this paper, a current stimulus is employed to emulate the external stimulus, and a second-order locally active memristor (LAM) is deployed to characterize the properties of ion channels. Then, a simple bionic circuit possessing the LAM, a capacitor, a DC voltage, and the current stimulus is constructed. Fast-slow dynamical effects of the current stimulus with low- and high-frequency are respectively explored. Numerical simulations disclose that the bionic circuit can generate bursting behaviors for the low-frequency current stimulus and spiking behaviors for the high-frequency current stimulus. Besides, fold and Hopf bifurcation sets are deduced and the bifurcation mechanisms for bursting behaviors are elaborated. Furthermore, the numerically simulated bursting and spiking behaviors are verified by PCB-based hardware experiments. These results reflect the feasibility of the bionic circuit in generating the firing patterns of spiking and bursting behaviors and the external current can be employed to regulate these firing patterns.

Introduction

Neurons are the basic functionality unit of the human brain, which possesses the most complex neural network in the world (Ison et al. 2015; Zyarah et al. 2020). The neuronal dynamics can influence the brain's functionalities, i.e., associate memory and cognitive behavior (Grewe et al. 2017; Wang et al. 2023; Shine et al. 2019; Andalman et al. 2019). The neurons act as signal receptors and processors with the firing patterns triggered by the changes in the electrophysiological environment (Lv et al. 2016; Li et al. 2024). The diversity of neuron firing patterns is crucial for realizing the brain's functionality and providing the basis for exploring brain-like applications (Sun et al. 2024; Wu et al. 2021). The bionic circuit is the hardware-bearing platform of the applications. Therefore, it is important to explore the production of abundant firing patterns and deduce their forming mechanism in the bionic circuit,

which can effectively reproduce various firing patterns or emulate the dynamical behaviors of neurons (Huang et al. 2019; Xu et al. 2024). In the literature, the bionic circuits were mainly constructed by considering the neuron functionality or neuronal microstructure. Some other bionic circuits were derived from neuron models by employing commercially available components, e.g., resistor, inductor, capacitor, and newly proposed circuit component, e.g., memristor (Xie et al. 2024a, b). In this paper, a bionic circuit is constructed by considering the micro-structure of the neuronal membrane, for which abundant firing patterns, e.g., fast-slow dynamics, related to external stimulus are revealed.

In 1952, Hodgkin and Huxley conducted a biometric experiment and acquired the membrane potential of the North Atlantic squid by current-clamp technique, and then built the first bionic circuit, aka, Hodgkin–Huxley (H–H) circuit, by the membrane theory (Hodgkin and Huxley 1952). Meanwhile, the ion transport mechanism for generating the membrane potential was elaborated (Hodgkin 1951). That is, the conductance of the sodium ion channel has a transient increase when sodium ions move inwards and the conductance of the potassium ion channel has a transient increase when potassium ions move outwards.

✉ Quan Xu
xuquan@cczu.edu.cn

1   School of Microelectronics and Control Engineering,
     Changzhou University, Changzhou 213159, China

The ion transport mechanism based on membrane theory declared that the action potential mainly depends on a rapid sequence of changes in the permeability to the sodium and potassium ions. They have declared that the conductances of the ion channels are time-varying and can be equivalent to time-varying resistors (Hodgkin and Huxley 1952). Following the pioneer's work, Professor Chua theoretically deduced that two time-varying resistors meet the definition of locally active memristor (LAM) (Jin et al. 2023; Lin et al. 2020).

The memristor was postulated in 1971 and widely deployed to construct memristive neuron models, neural networks (Li et al. 2024; Wang et al. 2024), and the echo state network (Deng et al. 2024). The concept of a LAM was introduced by Chua in 2014, which is associated with a device showing a negative differential resistance or negative differential conductance in its DC $V - I$ curve (Dong et al. 2020). LAM has the feature of amplifying small fluctuations in its locally active domain and triggering an action potential (Liang et al. 2020; Ying et al. 2023), which has natural advantages in constructing bionic circuits. According to the shapes of DC $V - I$ curves, the LAMs can be named voltage-controlled N-type LAM (Dong et al. 2022), current-controlled S-type LAM (Liang et al. 2020), voltage-controlled Chua corsage LAM (CCM) (Chua 2023), and CCM-like LAM (Xu et al. 2024). From the perspective of circuit modeling, N-type LAMs usually connect to a capacitor in parallel and S-type LAMs connect to an inductor in series. To date, LAMs were used to characterize the potassium ion and sodium ion channels in H–H circuits, from which the memristor parameters were adjusted to make the memristive H–H circuits exhibit periodic and chaotic firing patterns (Xu et al. 2024, 2019). Besides, LAM can be deployed to construct a bionic circuit via small signal analysis, which constructs Hopf bifurcation to make the bionic circuit lose its stability and generate spiking behaviors (Jin et al. 2021; Ascoli et al. 2022; Mannan et al. 2017).

Hardware implementation of the bionic circuits can verify the existence of firing patterns and provide the feasibility of applications. There are mainly three categories of physical implementation technologies, including the MCU- and FPGA-based digital platforms (Xu et al. 2023; Lin et al. 2023), CMOS-based VLSI circuits (Kumar et al. 2024; Guo et al. 2023), and commercially available component-based analog circuits (Xu et al. 2022, 2024). Each of these technologies possesses its features. The digital platforms can be flexibly modified by rewriting and updating code, but accuracy and adaptability should be considered. The CMOS-based VLSI circuit can provide high integration and energy efficiency but lacks the abilities of modification and universality. The commercially available component-based analog circuit has high design flexibility and good real-time performance, but it brings inevitable discreteness of circuit components. Besides, general researchers can perform commercially available component-based analog hardware measurements since there is a low requirement for experimental equipment.

Inspired by the above literature, this paper proposes a memristive ion channel-based bionic circuit, which involves an N-type LAM to characterize the ion channels, a capacitor to represent the membrane capacitor, a DC voltage to represent the reversal potential, and an AC current to emulate the external stimulus. The dynamical effect of the external stimulus is numerically and experimentally explored, since the firing pattern of a biological neuron is intimately related to changes in the electrophysiological environment (Yang et al. 2021; Wouapi et al. 2020; Ouyang et al. 2023). The most significant is that the bionic circuit can generate spiking behavior under the external stimulus with high-frequency and bursting behavior under low-frequency one. We name the dynamical effect of high- and low-frequency stimuli as fast-slow dynamics. Besides, the memristive ion channel-based bionic circuit might be more suitable to depict the firing patterns of a biological neuron.

The rest of this paper is arranged as follows. Section 2 deduces the modeling for the memristive ion channel-based bionic circuit and analyzes the equilibrium trajectory and its stability. In Section 3, bursting behaviors and their bifurcation mechanism are numerically revealed under the low-frequency stimulus, and then spiking behaviors and coexisting behaviors under the high-frequency stimulus are numerically disclosed. Section 4 performs the hardware experiments to verify the numerical results. Section 5 summarizes the paper.

Memristive ion channel-based bionic circuit

This section proposes an N-type second-order LAM and displays its memristive property and locally active domain. After that, the circuit schematic of the proposed bionic circuit is presented and the circuit state equation is built. Then, the equilibrium trajectory and the stability are studied.

An N-type second-order LAM

The commercially available component-based emulator of an N-type second-order LAM contains a floating ground module composed of current feedback operational amplifiers (C-FOAs) U_1 to U_4, two reverse integration circuit modules realized by two operational amplifiers (op-amps) U_A and U_B, an inverting adder module $-(+)$, and four

analog multiplier modules M_1 to M_4, as shown in Fig. 1 The floating module enables that the N-type LAM can connect to a DC voltage in series, which can ensure the LAM operating in its LAD. The N-type LAM includes two integration capacitor C_1 and C_2, where $v_{\varphi 1}$ is the state variable of C_1 and $v_{\varphi 2}$ is the state variable of C_2, and then its circuit state equation can be built as

$$
\begin{cases}
i_M = \dfrac{g_2(g_1 v_{\varphi 1} v_{\varphi 2} + v_{\varphi 2})v_M}{R_M} \\[2mm]
C_1 \dfrac{dv_{\varphi 1}}{dt} = \dfrac{g_3 v_{\varphi 1} v_M}{R_1} - \dfrac{v_{\varphi 1}}{R_2} - \dfrac{v_M}{R_3} \\[2mm]
C_2 \dfrac{dv_{\varphi 2}}{dt} = \dfrac{g_4 v_{\varphi 2} v_M}{R_4} - \dfrac{v_{\varphi 2}}{R_5} - \dfrac{v_M}{R_6}
\end{cases}
\tag{1}
$$

where i_M represents the current through the memristor and v_M denotes the input voltage of the memristor. g_1 to g_4 are the gains of the multipliers M_1 to M_4. Additionally, typical circuit parameters for the N-type LAM are chosen as

$C_1 = C_2 = 50\,\text{nF}$, $R_1 = R_6 = 1\text{k}\Omega$, $R_2 = R_5 = 2\text{k}\Omega$, $R_4 = 10\,\text{k}\Omega$, $R_3 = 20\text{k}\Omega$, $g_1 = g_2 = g_3 = g_4 = 1\ \text{V}^{-1}$, $R_W = R_{W1} = R_{W2} = 10\,\text{k}\Omega$, $R_M = 1\,\text{k}\Omega$.

The DC $V - I$ curve can obviously display the locally active property of a LAM (Chua 2022; Mannan et al. 2016). Herein, i_M and v_M are respectively denoted as I_M and V_M, and $dv_{\varphi 1}/dt = 0$, $dv_{\varphi 2}/dt = 0$ in Eq. (1) are set. By numerically calculating the relation between V_M and I_M, the DC $V - I$ curve is obtained, as shown in Fig. 2a. The DC $V - I$ curve exhibits a negative slope within the range of $0\,\text{V} \leq V_M \leq 0.4181\,\text{V}$ and has an N-shaped. The LAM can work in its LAD when series connecting to a DC voltage within this range. Figure 2b depicts frequency-dependent pinched hysteresis loops of the memristor, where $v_M = \sin(2\pi F t)$ is applied to the input terminal and the frequency F is set as 2, 5, and 10 kHz. It is demonstrated that the pinched hysteresis loops pass through the origin and the lobe area decreases with the increase of
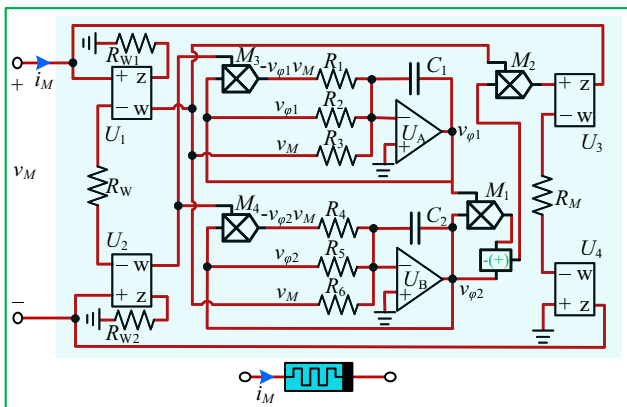
frequency, which meets the definition of a memristor (Chua 2015).

Circuit modeling and stability analysis

The memristive ion channel-based bionic circuit is newly constructed and its circuit scheme is figured out in the right of Fig. 3. The bionic circuit consists of an N-type second-order LAM W, a DC voltage E, a capacitor C, and a current stimulus I_{ext}. Herein, the concept of ion channel transport in membrane theory is employed to establish the memristive ion channel-based bionic circuit. The N-type LAM is a voltage-controlled one, which possesses an inner state variable with its resistance controlled by the input voltage and inner state variable. This can reflect the regulation of resistance in the interaction process of ion transport and membrane potential variation. Our aim is not to characterize the membrane structure of any specific biological neuron but to deploy the consideration of the membrane structure. Additionally, the relationship can be equivalently represented as parallel, since the ion channels of neurons are protein channels embedded in lipid bilayer membrane, as shown in the middle of Fig. 3. The mathematical state equation of the bionic circuit shown in Fig. 3 can be established as
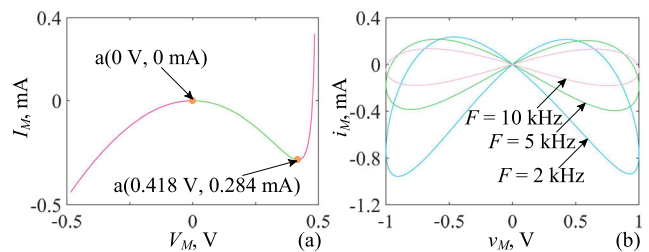

Fig. 2 Inner properties of the second-order LAM: **a** The DC V-I curve of the LAM; **b** Frequency-dependent pinched hysteresis loops of the LAM
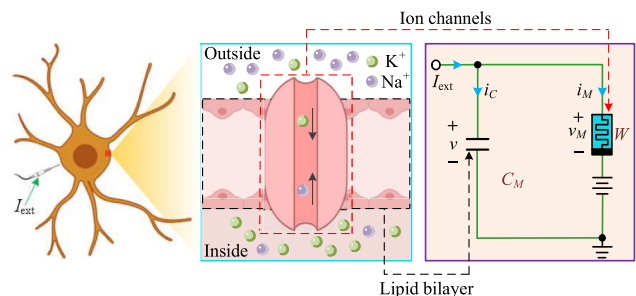

Fig. 3 Memristive ion channel-based bionic circuit

Fig. 1 Commercially available component-based emulator of the N-type second-order LAM

$$\begin{cases} C\dfrac{\mathrm{d}v}{\mathrm{d}t} = I_{\mathrm{ext}} - \dfrac{g_2(g_1v_{\varphi1}v_{\varphi2} + v_{\varphi2})(v - E)}{R_M} \\[2mm] C_1\dfrac{\mathrm{d}v_{\varphi1}}{\mathrm{d}t} = \dfrac{g_3v_{\varphi1}(v - E)}{R_1} - \dfrac{v_{\varphi1}}{R_2} - \dfrac{(v - E)}{R_3} \\[2mm] C_2\dfrac{\mathrm{d}v_{\varphi2}}{\mathrm{d}t} = \dfrac{g_4v_{\varphi2}(v - E)}{R_4} - \dfrac{v_{\varphi2}}{R_5} - \dfrac{(v - E)}{R_6} \end{cases} \quad (2)$$

Here, $C = 100$ nF and the external stimulus is given as $I_{\mathrm{ext}} = I_{\mathrm{m}}\sin(2\pi ft)$, where I_{ext} is the amplitude and f is the frequency. The DC voltage E is set to 0.3 V to push the LAM work in the LAD. Note that the bionic circuit has the natural frequency in about 1 kHz. This is a benefit for commercially available component-based hardware measurement. Certainly, we can regulate the natural frequency of the bionic circuit by adjusting the resistances and capacitances.

To analyze the equilibrium trajectory and its stability of the bionic circuit, we set the left side of Eq. (2) to 0 and the equilibrium trajectory E_S of the bionic circuit can be yielded as

$$E_S = \left[\eta, \frac{\eta - 0.3}{20(\eta - 0.8)}, \frac{10(\eta - 0.3)}{\eta - 5.3}\right] = [\eta, \chi_1, \chi_2] \quad (3)$$

where the value of the η can be solved by

$$I_{\mathrm{m}}\sin(2\pi ft) - \frac{(\chi_1\chi_2 + \chi_2)(\eta - 0.3)}{R_M} = 0 \quad (4)$$

Then, the Jacobian matrix at E_S can be expressed as

$$\mathbf{J}_S = \begin{pmatrix} m_{11} & m_{12} & m_{13} \\ m_{21} & m_{22} & 0 \\ m_{31} & 0 & m_{33} \end{pmatrix} \quad (5)$$

where

$$\begin{aligned} m_{11} &= -10000000(\chi_1\chi_2 + \chi_2)/R_M \\ m_{12} &= 10000000\chi_2(0.3 - \eta)/R_M \\ m_{13} &= 10000000(0.3 - \eta)(\chi_1 + 1)/R_M \\ m_{21} &= 20000\chi_1 - 1000 \\ m_{22} &= 20000\eta - 16000 \\ m_{31} &= 2000\chi_2 - 20000 \\ m_{33} &= 2000\eta - 10600 \end{aligned} \quad (6)$$

Thus, the characteristic polynomial of the Jacobian matrix is

$$\lambda^3 + m_1\lambda^2 + m_2\lambda + m_3 = 0 \quad (7)$$

Here

$$\begin{aligned} m_1 &= -m_{11} - m_{22} - m_{33} \\ m_2 &= m_{11}m_{22} - m_{12}m_{21} + m_{11}m_{33} - m_{13}m_{31} + m_{22}m_{33} \\ m_3 &= m_{12}m_{21}m_{33} - m_{11}m_{22}m_{33} + m_{13}m_{22}m_{31} \end{aligned}$$

$$(8)$$

A dynamical system can be regarded as slow variables modulating the fast variables when there exist more than two time scales (Han and Bi 2023). Herein, we set frequency f, which is much lower than the natural frequency of the bionic circuit. In this context, I_{ext} can be seen as a slow variable. That is, I_{ext} can be considered as a constant changing in $[-I_{\mathrm{m}}, I_{\mathrm{m}}]$. Here, we demonstrate the equilibrium trajectory and stability of the bionic circuit for $R_M = 0.5$ kΩ, $I_{\mathrm{m}} = 0.05$ mA and $f = 220$ Hz as a paradigm. Figure 4 illustrates the equilibrium trajectory of η value and its stability for the variation of current stimulus I_{ext}, within which different colors are deployed to represent different kinds of stability. One can see that there exist stable node focus (SNF) for $I_{\mathrm{ext}} < -0.5682$ mA and $I_{\mathrm{ext}} > -0.000006$ mA; unstable saddle point (USP) and SNF for -0.5682 mA $< I_{\mathrm{ext}} < -0.4949$ mA; unstable saddle focus (USF), USP, and SNF for -0.4949 mA $< I_{\mathrm{ext}} < -0.0180$ mA; SNF and USP for -0.0180 A $< I_{\mathrm{ext}} < -0.0078$ mA; SNF, USP, and stable node (SNP) for -0.0078 mA $< I_{\mathrm{ext}} < -0.000006$ mA; fold bifurcation points (FBP) for $I_{\mathrm{ext}} = -0.000006$ mA and $I_{\mathrm{ext}} = -0.5682$ mA; Hopf bifurcation point (HBP) for $I_{\mathrm{ext}} = -0.0180$ mA. In summary, the bionic circuit has three state variables possessing a similar time-scale, e.g., high-frequency, and fold/Hopf bifurcations for the variation of current stimulus. Thus, we can set the current stimulus with low-frequency to govern the bionic circuit having fast-slow time-scale, which can trigger bursting behaviors.
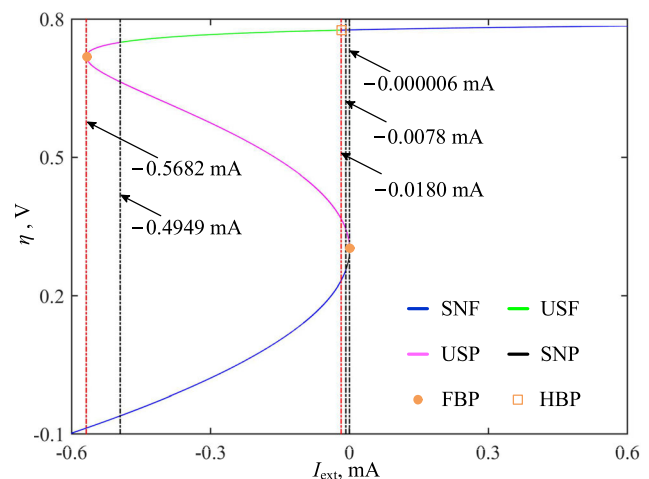

Fig. 4 Equilibrium trajectory and its stability with respect to I_{ext}

Fast-slow dynamical behaviors

External stimulus can effectively influence the electro-physiological activity of biological neurons (Kim et al. 2019; Yu et al. 2022; Sachdeva et al. 2020; Yao and Ma 2018). This section uses numerical simulations to explore the dynamical behavior of the memristive ion channel-based bionic circuit under high-frequency and low-frequency stimuli. In the numerical simulations, the MATLAB-based ODE45 algorithm with a total-time 0.1s and a fixed time-step 10^{-6}s are used to obtain the bifurcation diagram and time-domain waveform. Total-time 2 s and fixed time-step 10^{-4}s are set to calculate the Lyapunov exponent spectrum (LEs) by using the Jacobi matrix-based Wolf's method (Xu et al. 2023). The circuit parameters used in the dynamical analysis for low-frequency analysis are the same as those in the paradigm in Sect. 2. Additionally, the initial states are set to $[v(0), v_{\varphi 1}(0), v_{\varphi 2}(0)] = [0\,\text{V}, 0\,\text{V}, 0\,\text{V}]$ to eliminate the dynamical influence of initial states.

## Dynamical effect of low-frequency stimulus

The bifurcation diagram in a two-parameter plane can effectively reveal the dynamical distribution for the two parameters. By detecting the periodicity of state variable v, a two-parameter bifurcation diagram in the $I_m - f$ plane is plotted. Figure 5a shows the two-parameter bifurcation diagram in the interval of $0\,\text{mA} \leq I_m \leq 0.6\,\text{mA}$, $150\,\text{Hz} \leq f \leq 350\,\text{Hz}$ with $R_M = 0.5\,\text{k}\Omega$, in which different states are distinguished by different colors. These are, red for chaotic behavior(CH), yellow for multiple periodic behavior (MP) with its periodicity more than 8, and other colors for period-1 (P1) to period-8 (P8). Many stripe regions exist in the two-parameter bifurcation diagram, indicating the generation of rich dynamical behaviors. Figure 5b illustrates a two-parameter Lyapunov exponent plot in the $I_m - f$ parameter plane, which is described by the largest Lyapunov exponent. The colors are classified according to the values of the largest Lyapunov exponent. For a non-autonomous circuit, a positive Lyapunov exponent presents the chaotic state and a negative Lyapunov exponent stands for periodic states with different periodicities. One can observe that the Lyapunov exponent plot well confirms the dynamical behaviors revealed by the two-parameter bifurcation diagram. Note that the largest Lyapunov exponent is large in absolute value since the numerical simulation employs the state equation of a physical circuit with small time-scale (Chen et al. 2018).

Besides, the one-parameter bifurcation diagram and LEs plot are figured out to illustrate the bifurcation effects for one parameter, as shown in Fig. 6. The local maximum
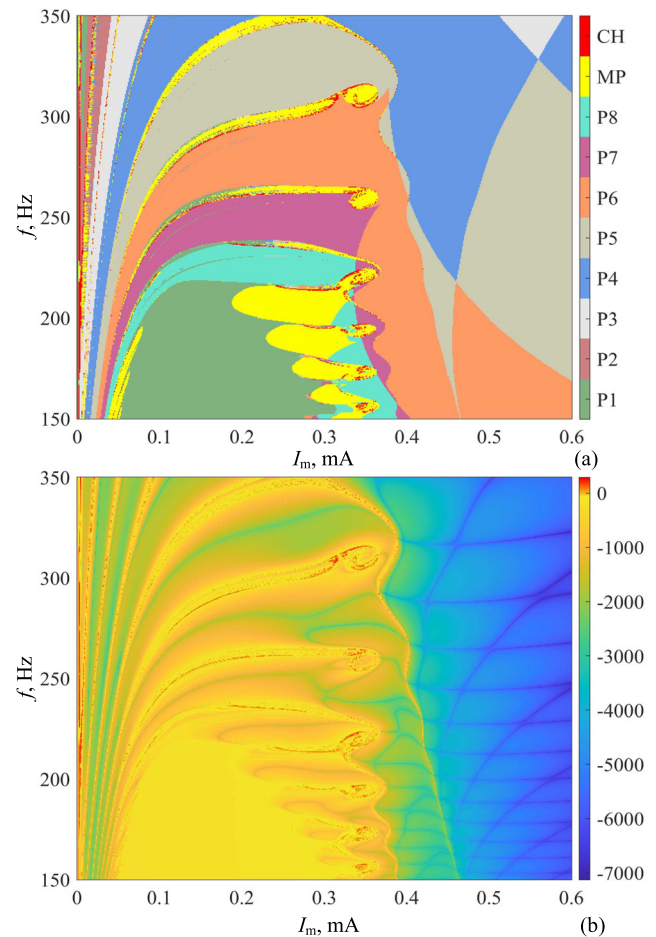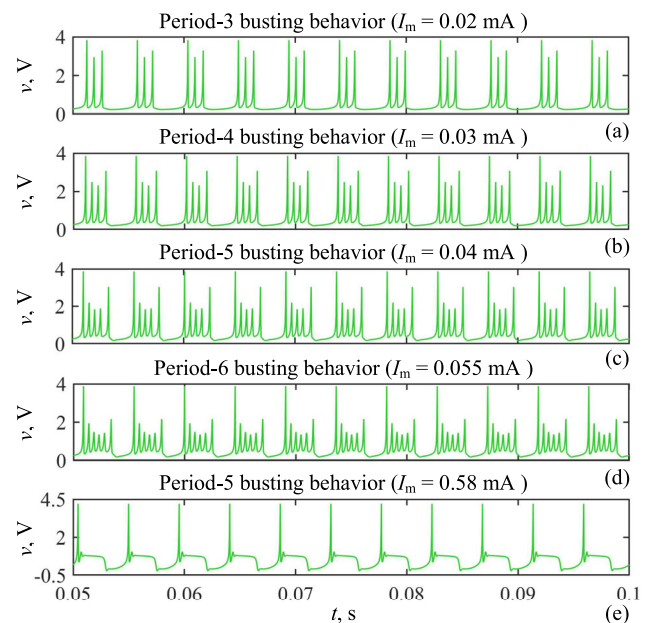

Fig. 5 Two-parameter dynamical distribution in the $I_m - f$ parameter plane, where $R_M = 0.5\,\text{k}\Omega$: **a** Two-parameter bifurcation diagram by checking the periodicity of v; **b** Two-parameter Lyapunov exponent plot described by the largest Lyapunov exponent

values of the state variable v is used to describe the one-parameter bifurcation diagram and the largest Lyapunov exponent is deployed in LEs plot. The upper of Fig. 6a displays the one-parameter bifurcation diagram as I_m varies in the interval $[0\,\text{mA}, 0.6\,\text{mA}]$ with $f = 220\,\text{Hz}$ and $R_M = 0.5\,\text{k}\Omega$. One can observe that period-adding bifurcation behaviors appear with the increase of I_m (Kafraj et al. 2020). Additionally, several narrow ranges of chaotic behavior exist within the parameter range $0.32\,\text{mA} \leq I_m \leq 0.36\,\text{mA}$, which is confirmed by the LE larger than zero, as shown in the bottom. Figure 6b illustrates the one-parameter bifurcation diagram and LEs plot by f varying in the interval $[150\,\text{Hz}, 350\,\text{Hz}]$ with $I_m = 0.05\,\text{mA}$ and $R_M = 0.5\,\text{k}\Omega$. The one-parameter bifurcation diagram and LEs plot in Fig. 6b demonstrate that reverse period-adding bifurcation behaviors are triggered with the increase of f and some narrow parameter ranges for chaos are generated, e.g., near $f = 215\,\text{Hz}$, $310\,\text{Hz}$, and $348\,\text{Hz}$.
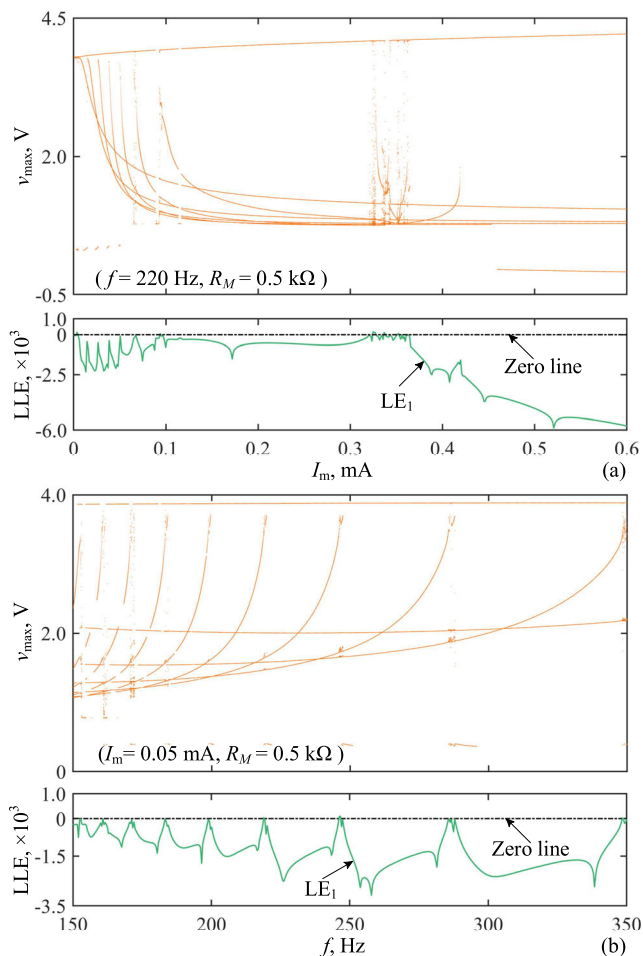
Fig. 6 One-parameter bifurcation diagrams(up) and LEs plot (bottom) for low-frequency stimulus, respectively: **a** For the variation of I_m; **b** For the variation of f


Fig. 7 Time-domain waveforms for different I_m with $f = 220$ Hz: **a** Period-3 bursting for $I_m = 0.02$ mA; **b** Period-4 bursting for $I_m = 0.03$ mA; **c** Period-5 bursting for $I_m = 0.04$ mA; **d** Period-6 bursting for $I_m = 0.055$ mA; **e** Period-5 bursting for $I_m = 0.58$ mA

The one-parameter bifurcation diagrams shown in Fig. 6 demonstrate that the bionic circuit can generate abundant periodic and chaotic firing patterns. To further disclose these firing patterns, we select some values of I_m from Fig. 6a and plot the time-domain waveforms of I_m, as shown in Fig. 7. The time-domain waveforms are P3 bursting, P4 bursting, P5 bursting, P6 bursting and P5 bursting, for $I_m = 0.02$ mA, $I_m = 0.03$ mA, $I_m = 0.04$ mA, $I_m = 0.055$ mA, and $I_m = 0.58$ mA, respectively. As I_m increases, the number of spikes in each burster increases, which verifies the period-adding bifurcation behavior. Note that period-5 bursting behaviors for $I_m = 0.04$ mA and $I_m = 0.58$ mA are different, which should be formed by different bifurcation mechanisms. Furthermore, these time-domain waveforms demonstrate that the memristive ion channel-based bionic circuit can effectively generate bursting behavior under the low-frequency stimulus. The membrane potential is not less than zero since the existence of DC voltage E. The DC voltage $E = 0.3$ V raises the

membrane potential to positive values. Note that our aim is not to replicate the firing patterns of any specific biological neuron. Instead, we are focusing on investigating the diverse firing patterns generated by the memristive ion channel-based bionic circuit.

Bifurcation mechanism for bursting behavior

Herein, we reveal the bifurcation mechanism of bursting behaviors by deducing the fold bifurcation (FB) and Hopf bifurcation (HB) sets of the bionic circuit. The polynomial equation in Eq. 7 has zero eigenvalue indicating the appearance of FB (Wouapi et al. 2021) and a pair of pure conjugate imaginary roots manifesting the occurrence of HB (Huang and Bi 2023). Thus, FB happens with $m_3 = 0$ and HB occurs with $m_3 = 0$ and $m_1 m_2 - m_3 = 0$. The FB and HB sets are figured out in Fig. 8. One can see that there is one FB for 0.000006 mA $< I_m < 0.018$ mA, one FB and one HB for 0.018 mA $< I_m < 0.5682$ mA, two FBs and one HB for 0.5682 mA $< I_m < 0.6$ mA respectively. This means that FB and HB happen two times with the number of them in a period of the stimulus, e.g., FB happens two times and HB happens two times in a period of the stimulus for $I_m = 0.04$ mA

To more intuitively reveal the bifurcation mechanism of bursting behaviors, time-domain waveforms of v along with the value of η of the equilibrium trajectory for $I_m = 0.04$ mA and $I_m = 0.58$ mA are selected as paradigms, as shown in Fig. 9. We describe the bifurcation mechanism
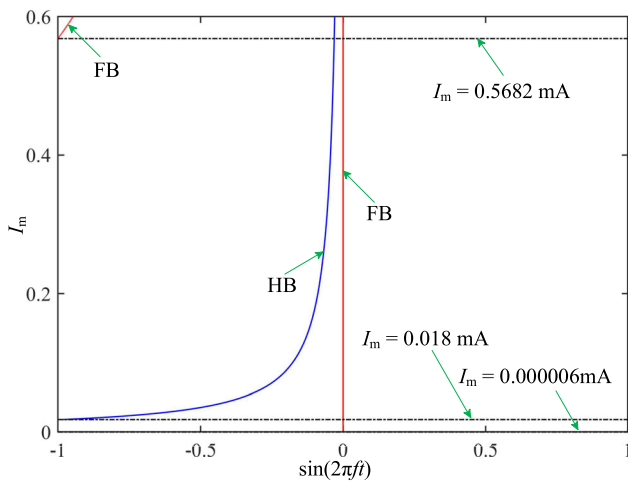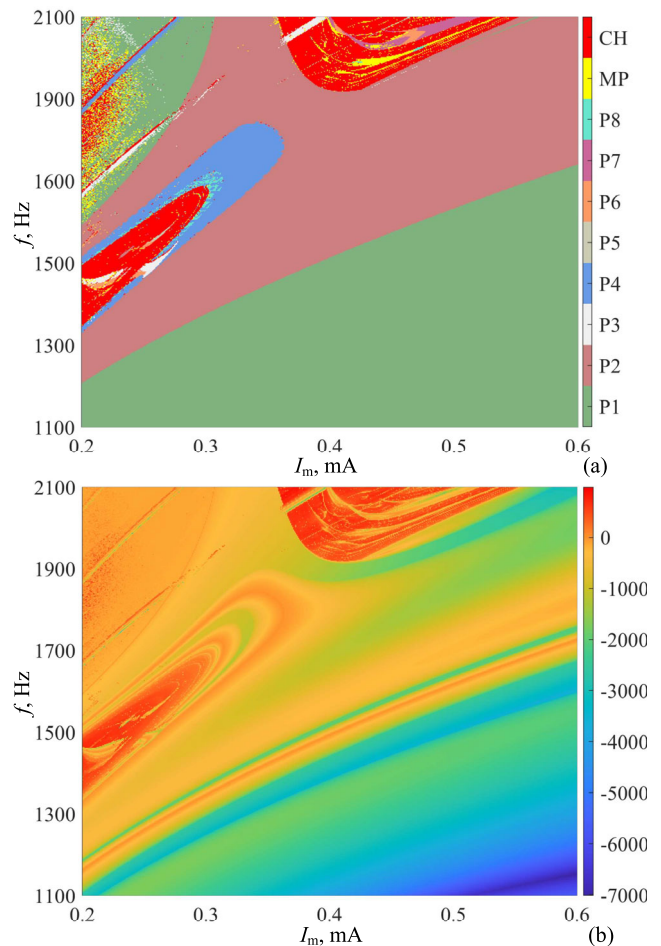
Fig. 8 FB and HB sets in the $\sin(2\pi ft) - I_m$ parameter plane
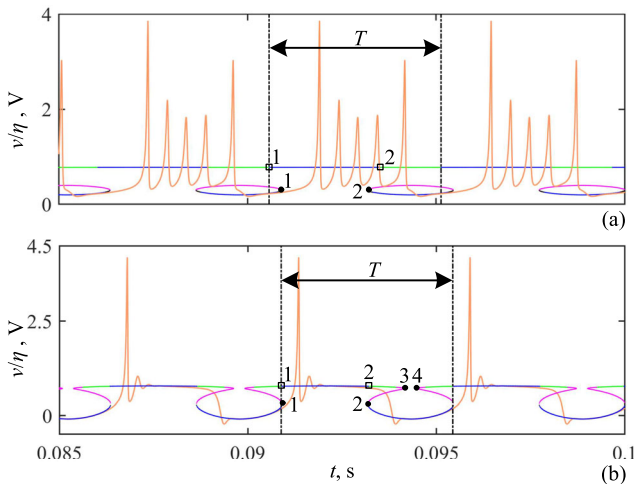
Fig. 9 Time-domain waveforms and equilibrium trajectories over the time: **a** $I_m = 0.04\,\text{mA}$; **b** $I_m = 0.58\,\text{mA}$

Fig. 10 Two-parameter dynamical distribution in the $I_m - f$ parameter plane with $R_M = 1\,\text{k}\Omega$: a Bifurcation diagram by checking the periodicity of v; b Lyapunov exponent plot

for the bursting behaviors in a period of the stimulus marked by T and the period is defined by starting at an HB point.

In Fig. 9a, the circuit trajectory initially operates along the lower SNF forming a resting state, then the HB **1** occurs. After that, the circuit trajectory only slightly deviates from the η-trajectory due to the coexistence of USP and SNP. The circuit trajectory transmits to the upper SNF and forms the spikes via FB **1**, and the amplitude of the spikes decreases since they oscillate along the upper SNF. Then, the amplitude of the spike increases when FB **2** happens along with the generation of USP. The amplitude of the spike further increases when HB **2** happens and the circuit trajectory transmits to the lower SNF exhibiting a resting state when the circuit trajectory passes through the SNF. Finally, the circuit trajectory enters into the next period T. In Fig. 9b, the bifurcation mechanism is the same

as the first case at the beginning and then the amplitude of the spike decreases to the upper SNF. After that, the circuit trajectory directly transmits to the lower SNF after the HB **2** happens. Then, the circuit trajectory falls into the lower SNF forming the resting state. In this process, the FB **2**, **3** and **4** do not affect the circuit trajectory.

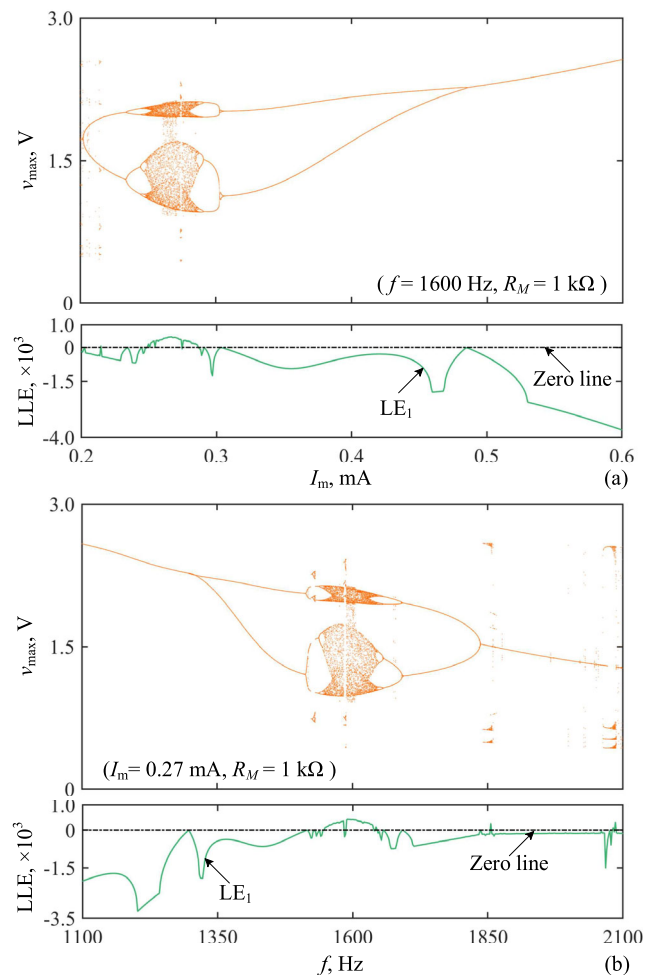## Dynamical effect of high-frequency stimulus

In this section, dynamical behaviors of the bionic circuit under high-frequency stimulus are investigated. The circuit parameters are set to $I_m = 0.27\,\text{mA}$, $f = 1600\,\text{Hz}$ and $R_M = 1\,\text{k}\Omega$ and the other circuit parameters are the same as the ones deployed in Sect. 3.1.

Two-parameter bifurcation diagram and Lyapunov exponent plot in the $I_m - f$ parameter plane are plotted. The adjustable parameter are set to $[0.2\,\text{mA}, 0.6\,\text{mA}]$ and $[1100\,\text{Hz}, 2100\,\text{Hz}]$ for I_m and f, respectively. The colormap setting for the bifurcation diagram is the same as the one

employed in Fig. 5. In Fig. 10a, there are extensive regions of chaotic behaviors and periodic behaviors blending into each other in the upper left parameter range. One can see that the memristive ion channel-based bionic circuit can exhibit various periodic and chaotic behaviors under different stimulus parameters. The two-parameter Lyapunov exponent plot in Fig. 10b further confirms the dynamical behaviors revealed by the bifurcation diagram.

Afterward, one-parameter bifurcation diagrams and LEs plots for I_m and f under high-frequency stimulus are numerically simulated, as shown in Fig. 11. In Fig. 11a, the bifurcation diagram shows a transition from MP to P2, then follows period-doubling bifurcations (Xu et al. 2023) demonstrating the dynamical transition of P4-P8-CH (Xu et al. 2023). Afterward, the reverse period-doubling bifurcation route happens, leading to the circuit trajectory running in P1. These dynamical transition behaviors are further confirmed by the corresponding one-parameter LEs plot. In Fig. 11b, the circuit trajectory starts with P1 and
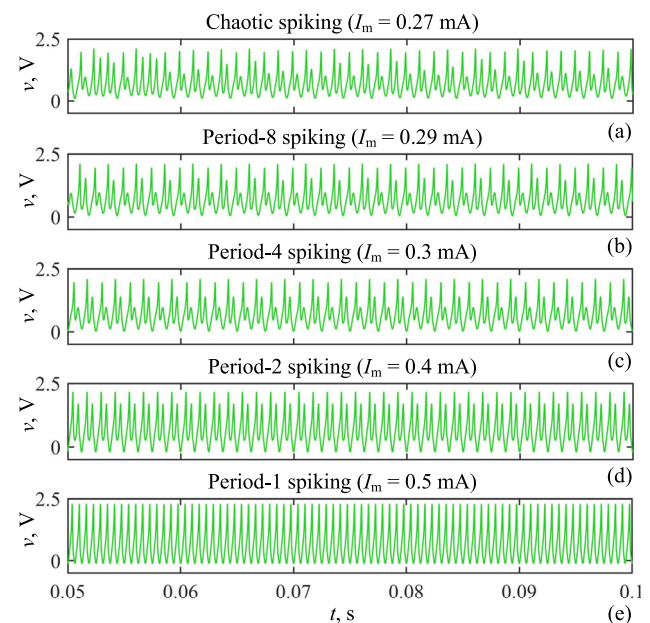
undergoes the period-doubling bifurcation route, leading the the occurrence of chaos. Then, the circuit trajectory falls into P1 via the reverse period-doubling bifurcation route. Notably, several sharp transitions occur during this evolution process, which might lead to the generation of coexisting behaviors related to memristor initial states. These sharp transitions are confirmed by the one-parameter LEs plot exhibiting several peaks above zero beyond the normal evolutionary trend.

To illustrate the firing patterns under the high-frequency stimulus, we selected some specific values of I_m to plot the time-domain waveforms of v, as shown in Fig. 12. They are chaotic spiking for $I_m = 0.27$ mA, period-8 spiking for $I_m = 0.29$ mA, period-4 spiking for $I_m = 0.3$ mA, period-2 spiking for $I_m = 0.4$ mA, and period-1 spiking for $I_m = 0.5$ mA. These time-domain waveforms display chaotic and periodic spiking behaviors, which are different from the bursting behaviors under the low-frequency stimulus. Besides, these firing patterns have a transition of CH-P8-P4-P2-P1, which further reflects the reverse period-doubling bifurcation route with the increase of I_m. These spiking firing patterns might hold the promise to provide high energy efficiency implementations of spike-based neuromorphic hardware for spiking neural networks (Abderrahmane et al. 2020).

The coexistence of firing patterns is an interesting phenomenon in biological neurons, which might play an unknown functionality in realizing biological information

Fig. 11 One-parameter bifurcation diagram (up) and LEs plot (bottom) for high-frequency stimulus: **a** For the variation of amplitude I_m; **b** For the variation of frequency f
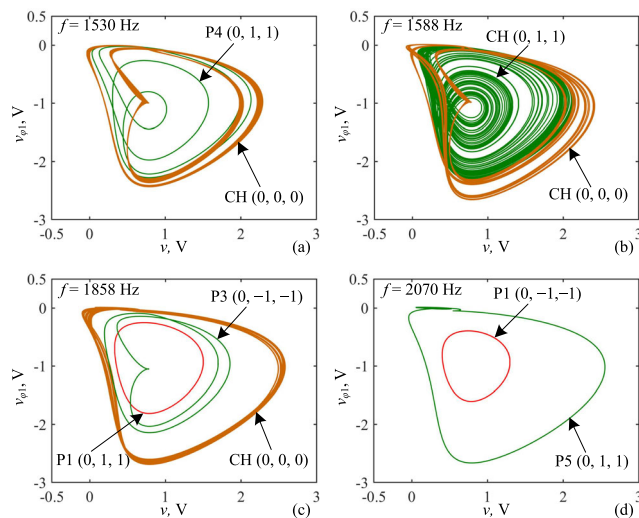

Fig. 12 Time-domain waveforms of v for different I_m with $f = 1600$ Hz: **a** Chaotic spiking for $I_m = 0.27$ mA; **b** Period-8 spiking for $I_m = 0.29$ mA; **c** Period-4 spiking for $I_m = 0.3$ mA; **d** Period-2 spiking for $I_m = 0.4$ mA; **e** Period-1 spiking for $I_m = 0.5$ mA

processing (Lin et al. 2021). In Fig. 11b, the single-parameter bifurcation diagram shows sharp transitions of dynamical behaviors, which implies the potential existence of coexisting firing patterns related to the initial states (Xu et al. 2024; Gu et al. 2015). Thus, we select four sets of circuit parameters in the sharp transition parameter ranges, e.g., $f = 1530\,\text{Hz}$, $f = 1588\,\text{Hz}$, $f = 1858\,\text{Hz}$, and $f = 2070\,\text{Hz}$ as paradigms to display the coexisting firing patterns. Phase trajectories in the $v - v_{\varphi 1}$ plane for the four sets of circuit parameters under different memristor initial states are figured out, as shown in Fig. 13. Figure 13a displays the coexisting P4 and CH firing patterns for $f = 1530\,\text{Hz}$ under initial states $[v(0), v_{\varphi 1}(0), v_{\varphi 2}(0)] = [0\,\text{V}, 1\,\text{V}, 1\,\text{V}]$ and $[0\,\text{V}, 0\,\text{V}, 0\,\text{V}]$. Figure 13b demonstrates the coexisting CH firing patterns for $f = 1558\,\text{Hz}$ under the initial states $[v(0), v_{\varphi 1}(0), v_{\varphi 2}(0)] = [0\,\text{V}, 1\,\text{V}, 1\,\text{V}]$ and $[0\,\text{V}, 0\,\text{V}, 0\,\text{V}]$. The two CH attractors have different topologies. Figure 13c demonstrates the coexisting P1, P3, and CH firing patterns for $f = 1858\,\text{Hz}$ under the initial states $[v(0), v_{\varphi 1}(0), v_{\varphi 2}(0)] = [0\,\text{V}, 1\,\text{V}, 1\,\text{V}]$, $[0\,\text{V}, -1\,\text{V}, -1\,\text{V}]$, and $[0\,\text{V}, 0\,\text{V}, 0\,\text{V}]$. Figure 13d gives the coexisting P1 and P5 firing patterns for $f = 2070\,\text{Hz}$ for initial states $[v(0), v_{\varphi 1}(0), v_{\varphi 2}(0)] = [0\,\text{V}, -1\,\text{V}, -1\,\text{V}]$ and $[0\,\text{V}, 1\,\text{V}, 1\,\text{V}]$. Actually, these are periodic and chaotic spiking behaviors.

Hardware circuit and experiment

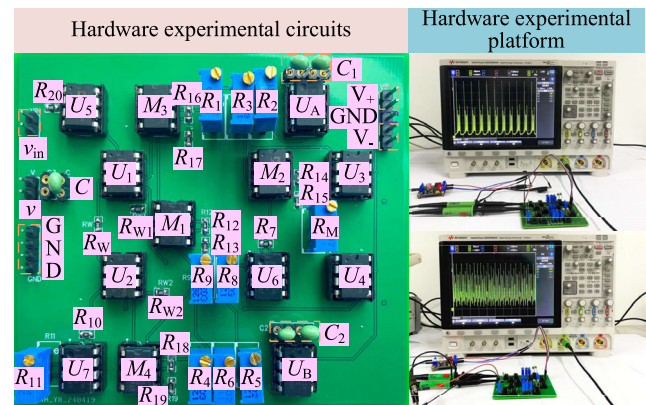The hardware experiment is crucial for confirming the dynamical behavior of a bionic circuit and verifying the feasibility of the bionic circuit. The hardware circuit using commercially available components is one of the feasible ways, which can offer some advantages, such as better real-time performance and design flexibility. In this section, we implement the memristive ion channel-based bionic circuit by discrete circuit components and execute hardware experiments to validate the numerical simulation results.

A discrete circuit component-based bionic circuit is made by referring to the equivalent circuit in Figs. 1 and 3, as depicted in the left of Fig. 14. In the hardware circuit, U_1 to U_5 are CFOA AD844AN, M_1 to M_4 are analog multiplier AD633JN, and U_A, U_B, U_6, and U_7 are operational amplifiers AD711JN. Among them, U_6 and R_7 to R_9 constitute an inverting adder module corresponding to the $-(+)$ module. U_7, R_{10}, and R_{11} are used to generate a DC voltage 0.3 V, R_{12} to R_{19} respectively control the gain of their connected multiplier to $1\,\text{V}^{-1}$. U_5 and R_{20} constitute a voltage-current conversion module, which converts the input AC voltage into AC current. Note that two 100 nF capacitors are connected in series to obtain the two capacitors $C_1 = 50\,\text{nF}$ and $C_2 = 50\,\text{nF}$. The DC voltage is connected to the LAM emulator in series to confirm the LAM working in its LAD. The right of Fig. 14 shows the hardware experimental platform. In hardware experiments, a TPS5420 voltage regulator module provides the $\pm 15\,\text{V}$ operating voltage. A function generator is employed to supply a sinusoidal AC voltage $V_{\text{ext}} = V_{\text{m}} \sin(2\pi f t)$. Then, the AC voltage is converted to AC current by using the voltage-current conversion module, and the conversion relationship is obtained as $I_{\text{ext}} = V_{\text{ext}}/10\,\text{k}\Omega$. An oscilloscope is connected to display the voltage of capacitor C.

Some circuit parameters are slightly adjusted to offset the parasitic parameters of discrete circuit components and the influence of the external environment (Wang et al. 2023; Cai et al. 2022; Xu et al. 2021). The other circuit parameters are set to the typical ones in numerical simulations. For low-frequency stimulus, I_{m}, R_M, R_1, R_2, and R_5 are finely adjusted to capture the time-domain waveforms

Fig. 13 Phase trajectories in the $v - v_{\varphi 1}$ plane for different f: **a** Coexisting P4 and CH for $f = 1530\,\text{Hz}$; **b** Coexisting CHs for $f = 1588\,\text{Hz}$; **c** Coexisting P1, P3 and CH for $f = 1858\,\text{Hz}$; **d** Coexisting P1 and P5 for $f = 2070\,\text{Hz}$

Fig. 14 Discrete circuit component-based hardware circuit (left) and hardware experimental platform (right)
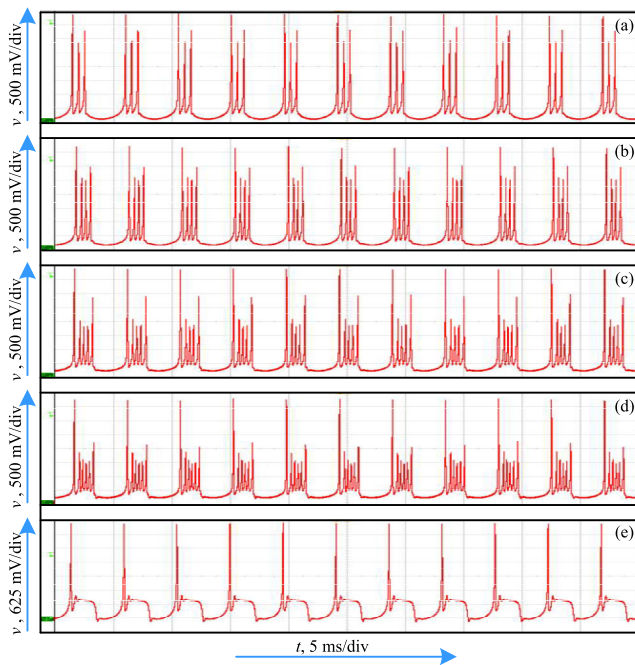
Fig. 15 Hardware measured time-domain waveforms of v for different I_m with $f = 220$ Hz: **a** Period-3 bursting for $I_m = 0.02$ mA; **b** Period-4 bursting for $I_m = 0.03$ mA; **c** Period-5 bursting for $I_m = 0.04$ mA; **d** Period-6 bursting for $I_m = 0.055$ mA; **e** Period-5 bursting for $I_m = 0.58$ mA

Fig. 16 Hardware measured time-domain waveforms of v for different I_m with $f = 1600$ Hz: **a** Chaotic spiking for $I_m = 0.27$ mA; **b** Period-8 spiking for $I_m = 0.29$ mA; **c** Period-4 spiking for $I_m = 0.3$ mA; **d** Period-2 spiking for $I_m = 0.4$ mA; **e** Period-1 spiking for $I_m = 0.5$ mA

for bursting behaviors, as shown in Fig. 15. The time-domain waveforms are shifted down by 2 V on the oscilloscope, except that P5 bursting behavior ($I_m = 0.58$ mA) is shifted down by 1.875 V for better visualization. For high-frequency stimulus, R_M, R_1, R_2, R_4, and R_5 are finely adjusted to capture the time-domain waveforms for spiking behaviors, as shown in Fig. 16. The time-domain waveforms are shifted down by 1.125 V on the oscilloscope.

Here, we assess the deviation of circuit parameters between hardware experiment and numerical simulation by the mean absolute percentage error (MAPE) (De Myttenaere et al. 2016), which can be written as

$$\text{MAPE} = \frac{1}{N}\sum_{k=1}^{N}\frac{|P_{\text{desired}k} - P_{\text{measured}k}|}{P_{\text{desired}k}} \times 100\% \qquad (9)$$

where $P_{\text{desired}k}$ is the circuit parameters in numerical simulation and $P_{\text{measured}k}$ is the circuit parameters in hardware experiment. N is the number of finely adjusted circuit parameters.

The finely adjusted circuit parameters and corresponding MAPEs for low-frequency and high-frequency stimuli are listed in Tables 1 and 2, respectively. They display that the MAPEs for low-frequency and high-frequency stimuli are all smaller than 10%, which is acceptable in analog circuit-based hardware experiments.
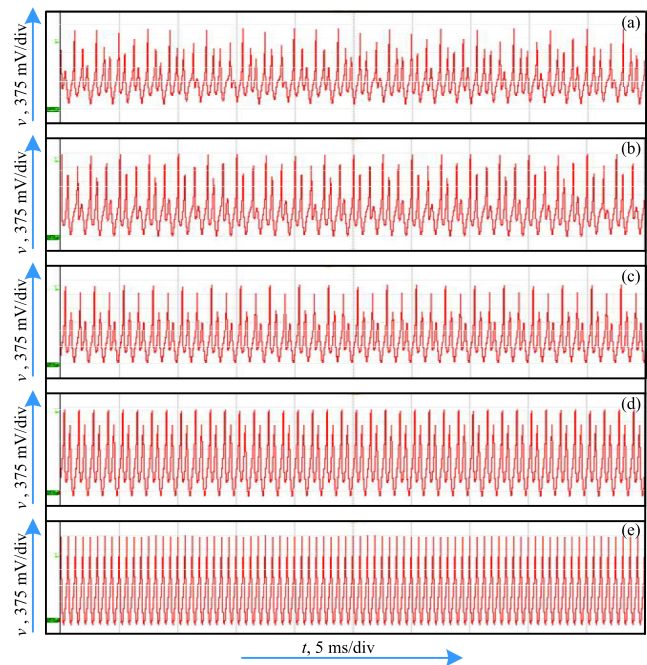
At low and high frequency stimulus, the MAPE values are respectively shown in Tables 1 and 2, with common fine-tunned parameters R_M, R_1, R_2, and R_5. The difference lies in the fact that for low frequency, fine-tunned parameters was done on the I_m, due to its smaller amplitude, whereas for high frequency, fine-tunned parameters was done on R_4. Seen from two tables, in the low-frequency experiments, as the number of periodicity for bursting behavior increases, the MAPE values exhibit a decreasing trend. However, in the high-frequency experiments, from P1 to CH spiking activities, the MAPE values show an increasing trend. The reason for this phenomenon can be found in the single-parameter bifurcation diagram with I_m, where wider ranges of I_m corresponding to the adjusted periodic behavior make hardware experiments relatively easier, and vice versa. This is also why period-8 spiking has the largest MAPE.

Conclusion

This paper proposed an N-type second-order LAM to characterize the ion channel of a neuronal membrane, thereby a memristive ion channel-based bionic circuit was constructed. The equilibrium trajectory and its stability of the bionic circuit have complex evolutions over time,

Table 1 Circuit parameters in hardware experiments and MAPEs for bursting behaviors

Bursting	Measured parameters (I_m, R_M, R_1, R_2, R_5)	MAPE
Period-3 busting	(0.023 mA, 0.52 kΩ, 1.05 kΩ, 2.21 kΩ, 1.85 kΩ)	8.4 %
Period-4 busting	(0.033 mA, 0.55 kΩ, 1.07 kΩ, 1.89 kΩ, 2.12 kΩ)	7.5 %
Period-5 busting	(0.041 mA, 0.56 kΩ, 0.97 kΩ, 2.11 kΩ, 2.08 kΩ)	5.4 %
Period-6 busting	(0.055 mA, 0.51 kΩ, 0.93 kΩ, 2.06 kΩ, 1.88 kΩ)	3.6 %
Period-5 busting	(0.58 mA, 0.48 kΩ, 1 kΩ, 2 kΩ, 2 kΩ)	0.8 %

Table 2 Circuit parameters in hardware experiments and MAPEs for spiking behaviors

Spiking	Measured parameters (R_M, R_1, R_2, R_4, R_5)	MAPE
Chaotic spiking	(0.89 kΩ, 0.85 kΩ, 2.14 kΩ, 9.90 kΩ, 2.13 kΩ)	8.1 %
Period-8 spiking	(0.87 kΩ, 0.90 kΩ, 2.19 kΩ, 10.67 kΩ, 2.15 kΩ)	9.3 %
Period-4 spiking	(1.10 kΩ, 0.92 kΩ, 1.94 kΩ, 10.35 kΩ, 2.08 kΩ)	5.7 %
Period-2 spiking	(0.96 kΩ, 0.94 kΩ, 1.95 kΩ, 10 kΩ, 1.92 kΩ)	3.3 %
Period-1 spiking	(1.05 kΩ, 0.96 kΩ, 2.04 kΩ, 10 kΩ, 1.92 kΩ)	3.0 %

which involve FBP and HBP. Numerical simulations and hardware experiments were performed to reveal the fast-slow dynamics in the bionic circuit. It is displayed that the bionic circuit can generate chaotic and periodic bursting behaviors when applying a low-frequency current stimulus. The FB/HB sets were numerically simulated and the bifurcation mechanisms for bursting behaviors were qualitatively deduced. Besides, chaotic/periodic spiking behaviors and coexisting firing patterns were disclosed when applying a high-frequency stimulus. These numerical simulations and hardware experiments verify the memristive ion channel-based bionic circuit can effectively generate chaotic/periodic busting and spiking behaviors.

The done work let us know that the N-type LAM is effective in characterizing ion channels to construct bionic circuits and generate firing patterns. We can deploy N-type LAMs with different mathematical models to extend the design of bionic circuits with this topology. In other words, the topology of the bionic circuit is extendable. Besides, ion channel blockage can affect the firing patterns (Zhou et al. 2020). How to characterize the ion channel blockage effect by an N-type LAM? These deserve our concern in future work.

Author contributions X. Ding: Writing—original draft, Methodology, Formal analysis. C. Feng: Formal analysis, Conceptualization. N. Wang: Writing—review & editing, Formal analysis. A. Liu: Software. Q. Xu: Writing—review & editing, Supervision.

Data availability The datasets generated during and/or analyzed during the current study are available from the corresponding author on reasonable request.

Declarations

Conflict of interest The authors declare that they have no Conflict of interest.

References

Abderrahmane N, Lemaire E, Miramond B (2020) Design space exploration of hardware spiking neurons for embedded artificial intelligence. Neural Netw 121:366–386

Andalman AS, Burns VM, Lovett-Barron M, Broxton M, Poole B, Yang SJ, Grosenick L, Lerner TN, Chen R, Benster T et al (2019) Neuronal dynamics regulating brain and behavioral state transitions. Cell 177(4):970–985

Ascoli A, Demirkol AS, Tetzlaff R, Chua L (2022) Edge of chaos theory resolves smale paradox. IEEE Trans Circuits Syst I 69(3):1252–1265

Cai J, Bao H, Chen M, Xu Q, Bao B (2022) Analog/digital multiplierless implementations for nullcline-characteristics-based piecewise linear Hindmarsh-Rose neuron model. IEEE Trans Circuits Syst I 69(7):2916–2927

Chen H, Bayani A, Akgul A, Jafari MA, Pham VT, Wang X, Jafari S (2018) A flexible chaotic system with adjustable amplitude, largest lyapunov exponent, and local kaplan-yorke dimension and its usage in engineering applications. Nonlinear Dyn 92:1791–1800

Chua L (2015) Everything you wish to know about memristors but are afraid to ask. Radioengineering 24(02):319–368

Chua LO (2023) Homemade US $10 Chua corsage memristor: Use it to make the poor man's biomimetic neurons. IEEE Electron Devices Mag 1(2):10–22

Chua L (2022) Hodgkin–Huxley equations implies edge of chaos kernel. Jpn J Appl Phys **61**(SM), SM0805

De Myttenaere A, Golden B, Le Grand B, Rossi F (2016) Mean absolute percentage error for regression models. Neurocomputing 192:38–48

Deng Q, Wang C, Sun J, Sun Y, Jiang J, Lin H, Deng Z (2024) Nonvolatile CMOS memristor, reconfigurable array, and its application in power load forecasting. IEEE Trans Ind Inf 20(4):6130–6141

Dong Y, Wang G, Liang Y, Chen G (2022) Complex dynamics of a bi-directional N-type locally-active memristor. Commun Nonlinear Sci Numer Simul 105:106086

Dong Y, Wang G, Iu HHC, Chen G, Chen L (2020) Coexisting hidden and self-excited attractors in a locally active memristor-based circuit. Chaos **30**(10)

Grewe BF, Gründemann J, Kitch LJ, Lecoq JA, Parker JG, Marshall JD, Larkin MC, Jercog PE, Grenier F, Li JZ et al (2017) Neural ensemble dynamics underlying a long-term associative memory. Nature 543(7647):670–675

Gu H, Pan B, Li Y (2015) The dependence of synchronization transition processes of coupled neurons with coexisting spiking and bursting on the control parameter, initial value, and attraction domain. Nonlinear Dyn 82:1191–1210

Guo C, Xiao Y, Jian M, Zhao J, Sun B (2023) Design and optimization of a new cmos high-speed H-H neuron. Microelectron J 136:105774

Han X, Bi Q (2023) Sliding fast-slow dynamics in the slowly forced Duffing system with frequency switching. Chaos Solit Fract 169:113270

Hodgkin AL (1951) The ionic basis of electrical activity in nerve and muscle. Biol Rev 26(4):339–409

Hodgkin AL, Huxley AF (1952) A quantitative description of membrane current and its application to conduction and excitation in nerve. J Physiol 117(4):500

Huang J, Bi Q (2023) Multiple modes of bursting phenomena in a vector field of triple Hopf bifurcation with two time scales. Chaos Solit Fract 175:113999

Huang L, Wu G, Zhang Z, Bi Q (2019) Fast-slow dynamics and bifurcation mechanism in a novel chaotic system. Int J Bifurc Chaos 29(10):1930028

Ison MJ, Quiroga RQ, Fried I (2015) Rapid encoding of new memories by individual neurons in the human brain. Neuron 87(1):220–230

Jin P, Wang G, Liang Y, Iu HHC, Chua LO (2021) Neuromorphic dynamics of Chua corsage memristor. IEEE Trans Circ Syst I 68(11):4419–4432

Jin P, Wang G, Chen L (2023) Biphasic action potential and chaos in a symmetrical Chua corsage memristor-based circuit. Chaos **33**(2)

Kafraj MS, Parastesh F, Jafari S (2020) Firing patterns of an improved Izhikevich neuron model under the effect of electromagnetic induction and noise. Chaos Solit Fract 137:109782

Kim JH, Lee JK, Kim HG, Kim KB, Kim HR (2019) Possible effects of radiofrequency electromagnetic field exposure on central nerve system. Biomol Ther 27(3):265

Kumar P, Ranjan RK, Kang SM (2024) A memristor emulation in 180-nm CMOS process for spiking signal generation and chaos application. IEEE Trans Circuits Syst I 71(4):1757–1770

Li Y, Ma J, Xie Y (2024) A biophysical neuron model with double membranes. Nonlinear Dyn 112(9):7459–7475

Li J, Wang C, Deng Q (2024) Symmetric multi-double-scroll attractors in Hopfield neural network under pulse controlled memristor. Nonlinear Dyn 112:14463–14477

Liang Y, Wang G, Chen G, Dong Y, Yu D, Iu HHC (2020) S-type locally-active memristor-based periodic and chaotic oscillators. IEEE Trans Circuits Syst I 67(12):5139–5152

Lin H, Wang C, Chen C, Sun Y, Zhou C, Xu C, Hong Q (2021) Neural bursting and synchronization emulated by neural networks and circuits. IEEE Trans Circuits Syst I 68(8):3397–3410

Lin H, Wang C, Sun Y, Yao W (2020) Firing multistability in a locally active memristive neuron model. Nonlinear Dyn 100(4):3667–3683

Lin H, Wang C, Yu F, Hong Q, Xu C, Sun Y (2023) A triple-memristor hopfield neural network with space multi-structure attractors and space initial-offset behaviors. IEEE Trans Comput-Aided Des Integr Circuits Syst 42(12):4948–4958

Lv M, Wang C, Ren G, Ma J, Song X (2016) Model of electrical activity in a neuron under magnetic flow effect. Nonlinear Dyn 85:1479–1490

Mannan ZI, Choi H, Kim H (2016) Chua corsage memristor oscillator via Hopf bifurcation. Int J Bifurc Chaos 26(04):1630009

Mannan ZI, Choi H, Rajamani V, Kim H, Chua L (2017) Chua corsage memristor: Phase portraits, basin of attraction, and coexisting pinched hysteresis loops. Int J Bifurcat Chaos 27(03):1730011

Ouyang G, Wang S, Liu M, Zhang M, Zhou C (2023) Multilevel and multifaceted brain response features in spiking, ERP and ERD: experimental observation and simultaneous generation in a neuronal network model with excitation-inhibition balance. Cogn Neurodyn 17(6):1417–1431

Sachdeva PS, Livezey JA, DeWeese MR (2020) Heterogeneous synaptic weighting improves neural coding in the presence of common noise. Neural Comput 32(7):1239–1276

Shine JM, Breakspear M, Bell PT, Ehgoetz Martens KA, Shine R, Koyejo O, Sporns O, Poldrack RA (2019) Human cognition involves the dynamic integration of neural activity and neuromodulatory systems. Nat Neurosci 22(2):289–296

Sun J, Li C, Wang Y, Wang Z (2024) Dynamic analysis of FN–HR neural network coupled of bistable memristor and encryption application based on Fibonacci Q-Matrix. Cogn Neurodyn pp. 1–18

Wang C, Liang J, Deng Q (2024) Dynamics of heterogeneous Hopfield neural network with adaptive activation function based on memristor. Neural Networks 178:106408

Wang N, Xu D, Kuznetsov N, Bao H, Chen M, Xu Q (2023) Experimental observation of hidden Chua's attractor. Chaos Solit Fract 170:113427

Wang C, Xu C, Sun J, Deng Q (2023) A memristor-based associative memory neural network circuit with emotion effect. Neural Comput Appl 35(15):10929–10944

Wouapi KM, Fotsin BH, Louodop FP, Feudjio KF, Njitacke ZT, Djeudjo TH (2020) Various firing activities and finite-time synchronization of an improved Hindmarsh-Rose neuron model under electric field effect. Cogn Neurodyn 14:375–397

Wouapi MK, Fotsin BH, Ngouonkadi EBM, Kemwoue FF, Njitacke ZT (2021) Complex bifurcation analysis and synchronization optimal control for Hindmarsh-Rose neuron model under magnetic flow effect. Cogn Neurodyn 15:315–347

Wu A, Chen Y, Zeng Z (2021) Quantization synchronization of chaotic neural networks with time delay under event-triggered strategy. Cogn Neurodyn 15:897–914

Xie Y, Wang X, Li X, Ye Z, Wu Y, Yu D, Jia Y (2024) Energy consumption in the synchronization of neurons coupled by electrical or memristive synapse. Chin J Phys 90:64–82

Xie Y, Ye Z, Li X, Wang X, Jia Y (2024) A novel memristive neuron model and its energy characteristics. Cogn Neurodyn 18:1989–2001

Xu Q, Fang Y, Feng C, Parastesh F, Chen M, Wang N (2024) Firing activity in an N-type locally active memristor-based Hodgkin-

Huxley circuit. Nonlinear Dyn. https://doi.org/10.1007/s11071-024-09728-z

Xu Q, Huang L, Wang N, Bao H, Wu H, Chen M (2023) Initial-offset-boosted coexisting hyperchaos in a 2D memristive Chialvo neuron map and its application in image encryption. Nonlinear Dyn 111(21):20447–20463

Xu Q, Ju Z, Ding S, Feng C, Chen M, Bao B (2022) Electromagnetic induction effects on electrical activity within a memristive Wilson neuron model. Cogn Neurodyn 16:1221–1231

Xu Q, Liu T, Ding S, Bao H, Li Z, Chen B (2023) Extreme multistability and phase synchronization in a heterogeneous bi-neuron Rulkov network with memristive electromagnetic induction. Cogn Neurodyn 17(3):755–766

Xu Q, Liu T, Feng CT, Bao H, Wu HG, Bao BC (2021) Continuous non-autonomous memristive Rulkov model with extreme multistability. Chin Phys B 30(12):128702

Xu Y, Ma J, Zhan X, Yang L, Jia Y (2019) Temperature effect on memristive ion channels. Cogn Neurodyn 13:601–611

Xu Q, Wang K, Chen M, Parastesh F, Wang N (2024) Bursting and spiking activities in a wilson neuron circuit with memristive sodium and potassium ion channels. Chaos Solit Fract 181:114654

Xu Q, Wang Y, Iu HHC, Wang N, Bao H (2023) Locally active memristor-based neuromorphic circuit: Firing pattern and hardware experiment. IEEE Trans Circuits Syst I 70(8):3130–3141

Xu Q, Wang Y, Wu H, Chen M, Chen B (2024) Periodic and chaotic spiking behaviors in a simplified memristive Hodgkin-Huxley circuit. Chaos Solit Fract 179:114458

Xu Q, Chen X, Wu H, Iu HHC, Parastesh F, Wang N (2024) Relu function-based locally active memristor and its application in generating spiking behaviors. IEEE Trans Circuits Syst II. https://doi.org/10.1109/TCSII.2024.3401860

Yang Y, Ma J, Xu Y, Jia Y (2021) Energy dependence on discharge mode of izhikevich neuron driven by external stimulus under electromagnetic induction. Cogn Neurodyn 15:265–277

Yao Y, Ma J (2018) Weak periodic signal detection by sine-wiener-noise-induced resonance in the Fitzhugh-Nagumo neuron. Cogn Neurodyn 12:343–349

Ying J, Min F, Wang G (2023) Neuromorphic behaviors of VO2 memristor-based neurons. Chaos Solit Fract 175:114058

Yu F, Shen H, Yu Q, Kong X, Sharma PK, Cai S (2022) Privacy protection of medical data based on multi-scroll memristive Hopfield neural network. IEEE Trans Netw Sci Eng 10(2):845–858

Zhou X, Xu Y, Wang G, Jia Y (2020) Ionic channel blockage in stochastic Hodgkin-Huxley neuronal model driven by multiple oscillatory signals. Cogn Neurodyn 14:569–578

Zyarah AM, Gomez K, Kudithipudi D (2020) Neuromorphic system for spatial and temporal information processing. IEEE Trans Comput 69(8):1099–1112